Abundances of transcripts, proteins, and metabolites in the cell cycle of budding yeast reveal coordinate control of lipid metabolism

Heidi M. Blank[a], Ophelia Papoulas[b,c], Nairita Maitra[a], Riddhiman Garge[b,c], Brian K. Kennedy[d,e,f], Birgit Schilling[f], Edward M. Marcotte[b,c,*], and Michael Polymenis[a,*]
[a]Department of Biochemistry and Biophysics, Texas A&M University, College Station, TX 77843; [b]Center for Systems and Synthetic Biology and [c]Department of Molecular Biosciences, University of Texas at Austin, Austin, TX 78712; [d]Departments of Biochemistry and Physiology, Yong Loo Lin School of Medicine, National University of Singapore, Singapore 117596; [e]Centre for Healthy Ageing, National University of Singapore, National University Health System, Singapore 117609; [f]Buck Institute for Research on Aging, Novato, CA 94945

ABSTRACT Establishing the pattern of abundance of molecules of interest during cell division has been a long-standing goal of cell cycle studies. Here, for the first time in any system, we present experiment-matched datasets of the levels of RNAs, proteins, metabolites, and lipids from unarrested, growing, and synchronously dividing yeast cells. Overall, transcript and protein levels were correlated, but specific processes that appeared to change at the RNA level (e.g., ribosome biogenesis) did not do so at the protein level, and vice versa. We also found no significant changes in codon usage or the ribosome content during the cell cycle. We describe an unexpected mitotic peak in the abundance of ergosterol and thiamine biosynthesis enzymes. Although the levels of several metabolites changed in the cell cycle, by far the most significant changes were in the lipid repertoire, with phospholipids and triglycerides peaking strongly late in the cell cycle. Our findings provide an integrated view of the abundance of biomolecules in the eukaryotic cell cycle and point to a coordinate mitotic control of lipid metabolism.

INTRODUCTION

Exemplified by the discovery of cyclin proteins (Evans *et al.*, 1983), identifying biomolecules whose abundance changes in the cell cycle has been a critical objective of cell cycle studies for decades. Recognizing such molecular landmarks in the cell cycle is a valuable, and often necessary, step for deciphering how and why cell cycle pathways are integrated.

Over the past 20 years, cell cycle-dependent changes in mRNA levels during the cell cycle of *Saccharomyces cerevisiae* have been comprehensively defined not only from several arrest-and-release synchronization approaches (Cho *et al.*, 1998; Spellman *et al.*, 1998; de Lichtenberg *et al.*, 2005; Pramila *et al.*, 2006; Granovskaia *et al.*, 2010) but also from elutriation (Spellman *et al.*, 1998;

Blank et al., 2017). Unlike transcript profiling, cell cycle-dependent proteomic and metabolomic changes have been more limited and challenging to interpret due to different or poor synchronization, lack of matched transcriptomic datasets, and divergent results among the various studies. For example, there has only been one mass spectrometry (MS)-based proteomic analysis of the budding yeast cell cycle, sampling cultures at four time-points after they were released from arrest (Flory et al., 2006). Remarkably few proteins had altered levels during the time course of that experiment, and there was no correlation with the available transcriptomic datasets (Flory et al., 2006). Hence, at least in S. cerevisiae, it is not clear to what extent protein abundances are dynamic in the cell cycle and how tightly they are linked to transcriptional changes, if at all.

The picture is not much clearer in other experimental systems. In fission yeast, two recent studies used highly similar arrest-and-release synchronization and protein labeling (stable isotope labeling by amino acids in the cell culture; Mann, 2006) methods, followed by MS, to probe cell cycle-dependent changes in the proteome. In one study, only a single protein changed in abundance more than twofold (Carpy et al., 2014), while in the other report, ~150 proteins did (Swaffer et al., 2016). Neither study had experiment-matched transcriptomic datasets. Previously, hundreds of transcripts were reported to be periodic in the cell cycle of fission yeast (Rustici et al., 2004; Oliva et al., 2005).

In human cells, several reports sampled the proteome in the cell cycle with MS, but there is little consensus among them (Dephoure et al., 2008; Olsen et al., 2010; Lane et al., 2013; Ly et al., 2014; Becher et al., 2018; Dai et al., 2018; Schillinger et al., 2018). The fraction of proteins identified as periodic ranged from ~5% (Ly et al., 2014) to >65% (Schillinger et al., 2018). Synchronization was mostly achieved by release from chemical arrest, but two studies also used elutriation (Ly et al., 2014; Dai et al., 2018). In the only report where an experiment-matched transcriptomic dataset was generated (Ly et al., 2014), the correlation with transcript abundance was positive ($\rho = 0.63$, based on the Spearman rank correlation coefficient). Some of the differences among the above studies may arise from the use of different cell lines, such as HeLa (Dephoure et al., 2008; Olsen et al., 2010; Lane et al., 2013; Becher et al., 2018), K562 (Dai et al., 2018), SW480 (Schillinger et al., 2018), or NB4 (Ly et al., 2014). However, even for the same cell line (HeLa), synchronization (release from thymidine block and nocodazole arrest) and point in the cell cycle (0.5 h after nocodazole arrest), the relative change in abundance of the 3243 proteins identified in common between the two studies (Olsen et al., 2010; Becher et al., 2018), were poorly correlated ($\rho = 0.245$, based on Spearman's rank correlation coefficient; see Materials and Methods).

In S. cerevisiae, metabolites have been measured in the cell cycle after arrest-and-release synchronization in minimal medium with ethanol as a carbon source, focusing on exogenous control of cell cycle progression and downstream effects on metabolism (Ewald et al., 2016). At the G1/S transition, it is generally thought that cyclin-dependent kinase activity triggers lipolysis (Kurat et al., 2009) and mobilizes storage carbohydrates (Ewald et al., 2016; Zhao et al., 2016) to provide resources for cell division. In other systems, there is evidence of cell cycle-dependent changes on metabolite levels for the green alga Chlamydomonas reinhardtii (Juppner et al., 2017), fly (Sanchez-Alvarez et al., 2015), and human HeLa cells (Atilla-Gokcumen et al., 2014; Scaglia et al., 2014; Ahn et al., 2017). Despite these advances, there has been no experiment-matched sampling of the transcriptome or proteome in any of these studies,

making it difficult to integrate these datasets with gene expression, at the mRNA or protein levels.

Here, for the first time in any system, we generated comprehensive datasets for RNAs, proteins, metabolites, and lipids from the same samples of S. cerevisiae cells progressing synchronously in the cell cycle. Importantly, these samples were from elutriated, unarrested cells, maintaining as much as possible the normal coupling between cell growth and division. We found that while there is a broad correlation between the relative abundances of mRNAs and their corresponding proteins, cell cycle-dependent changes in transcriptional patterns are significantly dampened at the proteome level. The cellular lipid profile is highly cell cycle regulated, with triglycerides and phospholipids peaking late in the cell cycle, together with protein levels of ergosterol biosynthetic enzymes, highlighting the importance of integrating multiple "omic" datasets to identify cell cycle-dependent cellular processes.

RESULTS

Samples for the multi-omic cell cycle analysis

To apply genomewide methods for the identification of cell cycle-dependent changes in the abundance of molecules of interest, one must first obtain highly synchronous cell cultures. Preferably, synchronization must be achieved in a way that minimally perturbs cellular physiology and the coordination between cell growth and division (Mitchison, 1971; Aramayo and Polymenis, 2017). When cells are chemically or genetically arrested in the cell cycle to induce synchrony, known arrest-related artifacts can bias the results (Mitchison, 1971; Ly et al., 2015; Aramayo and Polymenis, 2017). An alternative synchronization method is elutriation, a physical process that fractionates an asynchronous cell population by cell size and sedimentation density properties of the cells, with minimal perturbation of cellular functions (Lindahl, 1948; Creanor and Mitchison, 1979; Banfalvi, 2008). Hence, we used centrifugal elutriation to obtain our synchronous cell cultures (see Materials and Methods, and Figure 1A). Elutriation separates cells primarily based on size, and size is used as a normalizing reference across different elutriation experiments. We isolated 101 different elutriated cultures, which were combined into 24 pools, based on the size at which they were harvested. Hence, we generated a cell size series, spanning a range from 40 to 75 fL, sampled at approximately every 5-fL intervals. These 24 pools were processed as independent samples in all analytical downstream pipelines. For statistical analysis (e.g., with the bootstrap ANOVA), the 24 cell size pools were grouped in eight groups for each of the ~5-fL increments in the cell size series (see Figure 1A). The same 24 distinct pools were aliquoted as needed (see Materials and Methods) to generate the input samples for measurements of RNA (with RNAseq), proteins (with liquid chromatography tandem mass spectrometry [LC-MS/MS]), and metabolites with gas chromatography–time-of-flight mass spectrometry (GC-TOF MS for primary metabolites, hydrophilic interaction chromatography [HILIC]-QTOF MS/MS for biogenic amines, and Charged Surface Hybrid [CSH]-QTOF MS/MS for lipids).

To gauge the synchrony of our samples by microscopy, we used budding as a morphological landmark, which roughly coincides with the initiation of DNA replication in S. cerevisiae (Pringle and Hartwell, 1981). The percentage of budded cells across the cell size series (Figure 1B) rose steadily from ~0% in the smallest cells (at 40 fL), to > 80% at the largest cell size (75 fL). The cell size at which half the cells were budded (a.k.a. "critical size," a proxy for the commitment step START) in our cell size
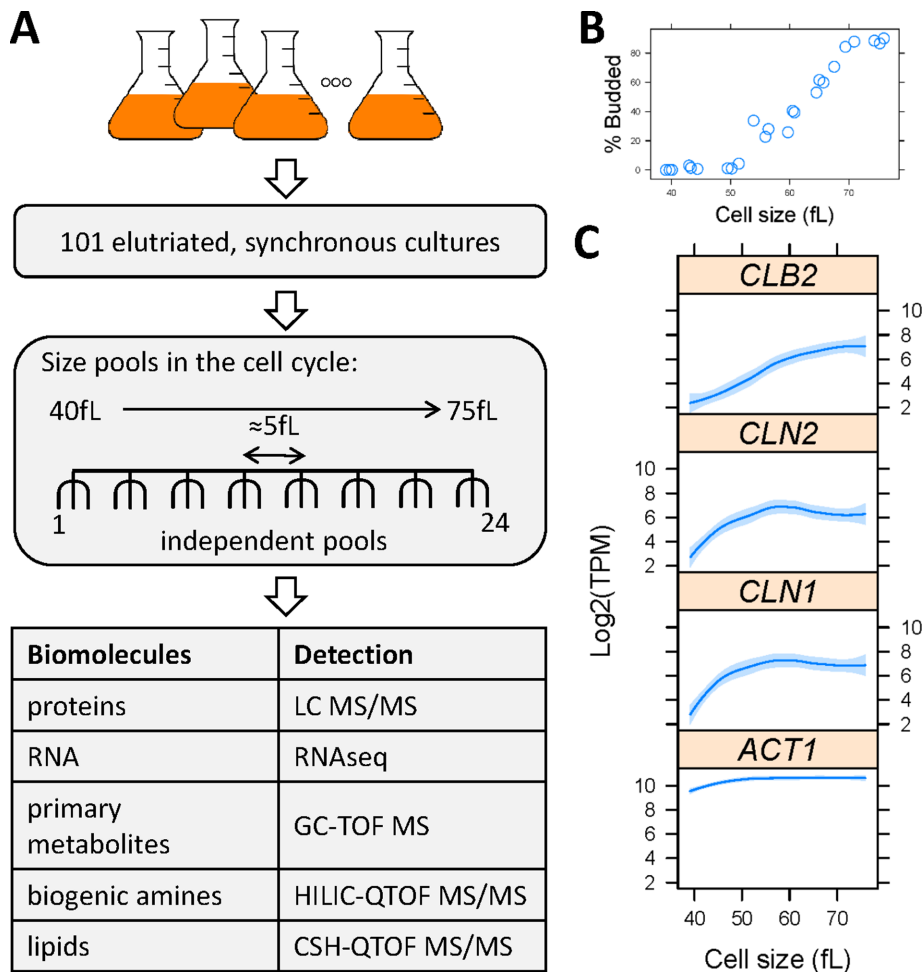
FIGURE 1: Overview of the experimental design to query cell cycle-dependent changes in the levels of RNAs, proteins, and metabolites. (A) Generation of sample-matched, multi-omic datasets from synchronous cultures of cells of different size during the cell cycle. (B) Serving as a morphological marker of cell cycle progression, the percentage of budded cells (*y*-axis) as a function of cell size (*x*-axis) is shown for each cell size pool. Cell size corresponds to the mean cell size of the population, and in this case it is the weighted average of all the mean cell sizes of all the elutriated samples that constituted each of the 24 pools. (C) The levels of mitotic (*CLB2*) or G1 (*CLN1,2*) cyclin mRNAs, which are known to be periodic in the cell cycle, are shown along with those of a nonperiodic transcript (*ACT1*; encoding actin). Cell size is shown on the *x*-axis (in fL), while the Log2-transformed TPM values for each transcript are shown on the *y*-axis. All 24 values, one for each pool, were plotted in these graphs. Loess curves and confidence bands indicating the standard errors on the curve at a 0.95 level were drawn using the default settings of the panel.smoother function of the *latticeExtra* R language package.

Overview of the data sets

One type of extract was analyzed for each class of the following biomolecules: RNA, primary metabolites, biogenic amines, and lipids (see *Materials and Methods* and Supplemental Table S1). For proteomic analysis, we used soluble protein extracts (designated as "sol" in the datasets; see Supplemental Table S1) and material from the same extract that was recovered in an insoluble pellet (designated as "pel" in the datasets, see Supplemental Table S1). The pellet was subsequently solubilized with detergents (see *Materials and Methods*) and analyzed in parallel to the soluble sample by LC-MS/MS. For label-free relative quantification of proteins, we used both spectral counts (designated as "psm" in the datasets; see Supplemental Table S1) and peak areas (designated as "pa" in the datasets; see Supplemental Table S1). For RNAs, the signal we used for quantification was read counts, either raw or after normalization as transcripts per kilobase million (TPM) (see *Materials and Methods* and Supplemental Table S1). For the metabolites, the signal was the peak heights from MS (designated as "ph" in the datasets; see Supplemental Table S1). The raw values for all datasets are in Supplemental File S1.

For the quantification of proteins and metabolites, each dataset was first normalized for input. Hence, for proteins or metabolites, comparisons across the 24 samples were scaled based on the sum of the signals detected in each of the 24 samples. For RNA, we used TPM-normalized values and raw reads (see Supplemental Table S1). All input datasets that entered the downstream computational analyses are in Supplemental File S2. For each dataset, we used a bootstrap-based ANOVA (see *Materials and Methods*; the output files are named as "anova" in the datasets; see Supplemental Table S1). Also, for RNA, we used the *DESeq2* pipeline ((Love *et al.*, 2014); see *Materials and Methods*; the output file is designated as "deseq2;" see Supplemental Table S1). All output datasets are in Supplemental File S3. Only biomolecules that changed ≥2-fold in our cell size series *and* had an adjusted *p* value or FDR <0.05 were considered as significantly changing in the cell cycle.

For display purposes, in all the heatmaps and most plots, we show Log2-transformed expressed ratio values. These are the ratios of the levels that we measured for each biomolecule in each cell cycle point, reflecting the magnitude of the ratio of abundance relative to the average of that biomolecule across all the cell cycle points we sampled. This approach was originally used to describe microarray cell cycle experiments in yeast (Spellman *et al.*, 1998) and has been the standard in displaying and analyzing differential expression in the cell cycle.

series was ~62 fL (Figure 1B). This value is the same as the critical size these cells display in typical time-series experiments (Hoose *et al.*, 2012). We also measured the DNA content of the cells with flow cytometry (Supplemental Figure S1). These results suggest that the synchrony is excellent for most of the cell cycle, except perhaps in the last one to two pools, when the cells have grown substantially in size and they are more heterogeneous. From the RNAseq data that we will describe later (Figure 2), mRNAs that are known to increase in abundance at the G1/S transition (G1 cyclins; *CLN1,2*; peaking at 55 fL), or later in G2 phase (cyclin *CLB2*; peaking at 70 fL), peaked as expected in the cell size series (Figure 1C). Hence, based on cytological (Figure 1B and Supplemental Figure S1) and molecular (cyclin mRNAs, Figure 1C) markers of cell cycle progression, the synchrony of our samples was of high quality.
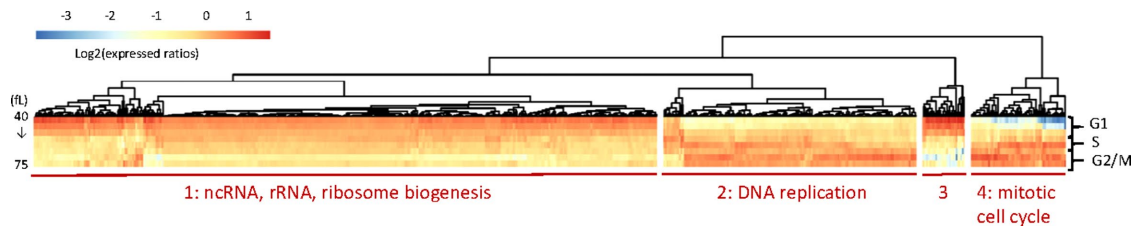
FIGURE 2: Transcripts changing in abundance in the cell cycle. Heatmap of the levels of 652 differentially expressed RNAs with significantly different levels ($p < 0.05$; Log2(FC) $\geq$ 1) between any two points in the cell cycle, based on bootstrap ANOVA. The levels of each RNA were the average of each triplicate for the cell size indicated, which was then divided by the average value of the entire cell size series for that RNA. These expressed ratios were then Log2-transformed. The Log2(expressed ratios) values were hierarchically clustered and displayed with the *pheatmap* R language package, using the default unsupervised algorithms of the package. The different rows of the heatmap correspond to the different cell sizes (40–75 fL, top to bottom, in 5-fL intervals). The cell cycle phases approximately corresponding to these sizes are shown to the right of the heatmap. The names of all RNAs, values, and clustering classifications are in Supplemental File S4/Sheet: rnas_anova_heatmap. The gene ontology enrichment analysis for each cluster was done on the PANTHER platform, and the detailed output is in Supplemental File S4/Sheet: rnas_clusters.

RNAs in the cell cycle

The RNAseq data were analyzed (see *Materials and Methods*, Figure 2, and Supplemental Table S1) to identify RNAs that change in abundance in the cell cycle. The names of all the RNAs in each set are shown in Supplemental File S4/Sheet: rna_sets. The number of identified RNAs varied, depending on the computational method. Based on the *DESeq2* approach, ~40% of the transcripts ($n = 2456$) were significantly different between any two points in the cell cycle. The ANOVA-based approach identified 652 RNAs, whose levels changed significantly in the cell size series (Figure 2). In addition to the expected clusters of RNAs associated with DNA replication (cluster 2) and mitotic cell cycle progression (cluster 4), there was a large cluster of transcripts enriched for processes related to ribosome biogenesis (cluster 1, Figure 2; see also Supplemental File S4), peaking in the G1 phase. These transcripts also appeared periodic in past studies that relied on elutriation as a synchronization method to identify cell cycle-regulated RNAs (Spellman *et al.*, 1998; Blank *et al.*, 2017), but not in studies that used arrest-and-release methods (Spellman *et al.*, 1998). An increase in the levels of transcripts involved in ribosome biogenesis before commitment to division has also been described in transcriptomic profiles of *S. pombe* (Oliva *et al.*, 2005). Despite these changes at the transcript level, whether the ribosome content of the cell changes during the cell cycle is not known. We will describe results that do not support any cell cycle-dependent changes in assembled ribosomes later.

Early in the cell cycle (clusters 1 and 3, Figure 2), we noticed that there were some tRNAs whose levels were higher. Note that tRNAs were not examined in the two prior studies that queried the transcriptome of elutriated *S. cerevisiae* cells because those studies focused on polyA-tailed selected transcripts (Spellman *et al.*, 1998; Blank *et al.*, 2017). It has been argued that polyA selection biases the transcriptome quantification (Weinberg *et al.*, 2016). Hence, in this study, we relied only on rRNA subtraction to prepare the RNAseq libraries (see *Materials and Methods*), which does not remove tRNAs and other noncoding RNAs. We also note that tRNAs are notoriously difficult to measure by RNAseq due to factors such as their high level of modification, sequence similarity between different tRNAs, and the difficulty to discriminate between cleaved and mature tRNAs. The tRNAs whose levels appeared to change in the cell cycle are shown in Supplemental Figure S2. These results are difficult to reconcile with the extreme stability of mature tRNAs (from 9 h to several days, exceeding the duration of multiple cell

cycles; see Hopper, 2013), unless these tRNAs are targets of quality control mechanisms (Hopper, 2013). In any case, as we show later (Supplemental Figure S8), we found very little evidence to support a significant role for altered codon usage in the cell cycle.

Last, we also compared the identified cell cycle genes from the two elutriation datasets published previously (Spellman *et al.*, 1998; Blank *et al.*, 2017) and in this study (Supplemental Figure S3 and File S7). The overlap in the identified cell cycle transcripts appears low (e.g., the Spellman dataset overlaps ≈20% with either of the other two datasets). However, different methods in sample preparation (total RNA in this study vs. polyA-selected mRNAs in the other two) and in the computational analyses (ANOVA in this study vs. Fourier transformation in the other two) were used, which could account at least in part for the differences.

Cell cycle-dependent changes in the proteome

From the soluble and insoluble extracts (see *Materials and Methods*), we identified 3571 *S. cerevisiae* proteins at one or more cell cycle points. From the soluble extracts, 2236 proteins were identified in all eight cell size groups in the cell cycle, while from the insoluble ones that number increased to 2449 proteins. Although this represents a reasonably thorough sampling of the yeast proteome, we did not find some low abundance proteins (e.g., cyclins). This was not unexpected, since a recent, aggregate analysis of all available datasets of protein abundances in yeast (measured with tandem affinity purification (TAP), followed by immunoblot analysis-, MS-, and GFP tag-based methods), placed proteins of the gene ontology process "mitotic cell cycle regulation" as the least abundant group (Ho *et al.*, 2018). The extent to which mRNA levels can explain protein levels is debated (Lu *et al.*, 2007; Vogel and Marcotte, 2012; Csardi *et al.*, 2015; Lahtvee *et al.*, 2017). For most species, RNA levels explain between one-third to two-thirds of the variation in protein abundances (Vogel and Marcotte, 2012). To examine the broad correlation between transcript and protein levels, we looked at the association of count data from our transcriptomic (reads) and proteomic (spectral counts) datasets (Supplemental Figure S4). Across all the points in our cell size series, the Spearman rank coefficients (ρ) for the transcriptome-proteome correlations ranged from 0.52 to 0.63 (Supplemental Figure S4). When we compared the relative abundance of the proteins in our datasets, against the consensus abundances calculated by (Ho *et al.*, 2018), the correlation was higher ($\rho > 0.75$ in every case; see Supplemental Figure S5 and File S8). Hence, both in terms of the number of proteins we identified
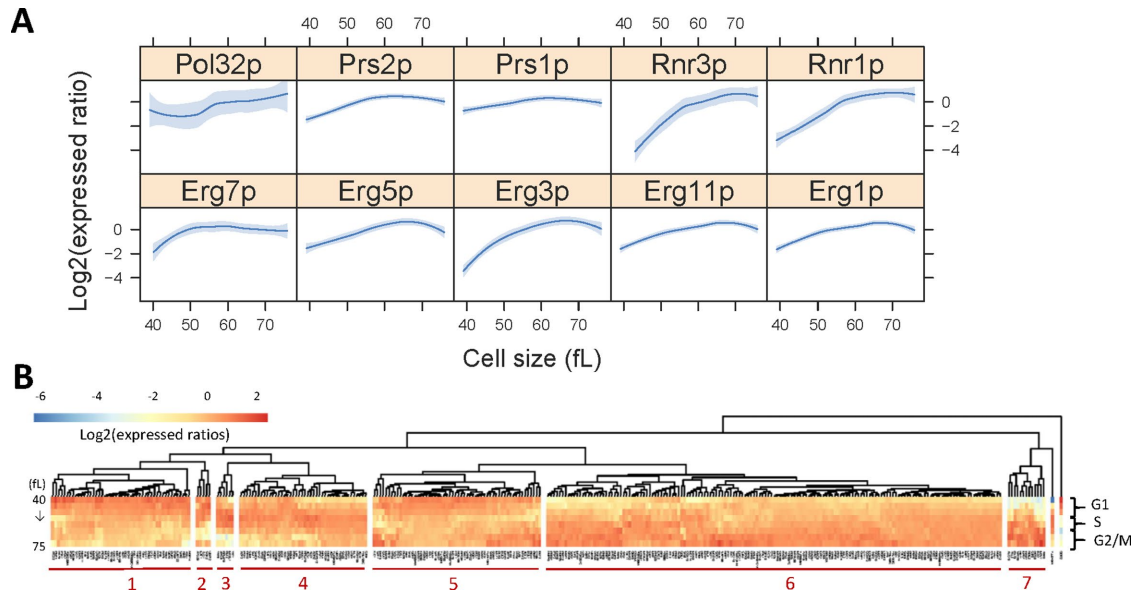
FIGURE 3: Proteins with cell cycle-dependent abundance. (A) Levels of selected proteins whose levels changed significantly ($p < 0.05$; Log2(FC) $\geq$ 1) between any two points in the cell cycle, based on bootstrap ANOVA, in the cell cycle: Bottom, enzymes involved in ergosterol biosynthesis. Top, enzymes involved in DNA metabolism (Pol32p: DNA polymerase δ; Prs1,2p: PRPP synthase; Rnr1,3p: ribonucleoside-diphosphate reductase). The corresponding Log2(expressed ratios) values from all 24 data points are on the y-axis, and cell size values are on the x-axis. Loess curves and confidence bands indicating the standard errors on the curve at a 0.95 level were drawn using the default settings of the panel.smoother function of the *latticeExtra* R language package. (B) Heatmap displaying the relative abundance of the 333 proteins in one or more of the four anova sets shown in Supplemental Figure S6. In cases where the same protein was in the intersection of more than one datasets, we chose for display the values from the dataset from which the changes in the protein abundance in the cell cycle was the most significant (i.e., the lowest p value) and greater in magnitude (i.e., the highest Log2(FC)). The heatmap was generated as in Figure 2. All the relevant data are in Supplemental File S4/Sheet: proteins_anova_heatmap.

and their relative abundance, the quality of our proteomic datasets was high and consistent with past studies.

To identify proteins that changed in abundance in the cell cycle, we examined separately each of the four proteomic datasets: soluble and insoluble extracts, each quantified by spectral counts and by peak areas (see Supplemental Table S1 and *Materials and Methods*). The overlap between the proteins in each dataset that appeared to change in abundance in the cell cycle was minimal (see Supplemental Figure S6). Based on ANOVA analysis, we identified 333 proteins whose levels changed significantly in the cell size series, in at least one of the four proteomic datasets (shown in the heatmap in Figure 3B). We will describe additional proteins whose levels change significantly in the cell cycle, but due to irregular patterns and missing values, they were not identified as such by the ANOVA-based method we used.

Our analysis provided numerous examples of physiologically relevant, cell cycle-dependent changes in protein abundance. Among these were several whose levels are well known to be periodic at both the protein and the RNA levels. These include proteins involved in DNA replication-related processes, such as both isoforms (Rnr1p and Rnr3p) of the large subunit of ribonucleoside-diphosphate reductase, peaking as cells enter S phase (Figure 3A, top). However, other groups of proteins that we found to change in abundance in the cell cycle were not so at the RNA level. For example, several enzymes of ergosterol biosynthesis (Erg1,11,3,5,7p) peaked late in the cell cycle (Figure 3A, bottom). Of those, only the levels of the mRNA for Erg3p (C-5 sterol desaturase) changed in the cell cycle (see Supplemental File S4/Sheet: rnas_anova_heatmap). The coordinate up-regulation in the levels of enzymes involved in

ergosterol biosynthesis is consistent with the mitotic increase in lipid levels that we will describe later.

Despite the transcriptional up-regulation in G1 of transcripts involved in ribosome biogenesis (see Figure 2), we did not observe such broad changes at the proteomic level. In earlier reports, the synthesis of ribosomal components was not cell cycle-dependent (Shulman *et al.*, 1973; Elliott *et al.*, 1979; Warner, 1999). To our knowledge, however, it is not known if the ribosome content in the cell, or the composition of ribosomal proteins in assembled ribosomes, changes in the cell cycle. Hence, we asked if the total amount of ribosomal proteins or their proportion in assembled ribosomes varies significantly in the cell cycle. To this end, we isolated assembled ribosomes through sucrose ultracentrifugation from wild-type cells (Figure 4A; see *Materials and Methods*). Ribosomal protein abundance was measured with SWATH-MS (see *Materials and Methods*). Note that for this experiment, extracts were not made from pools of different elutriated cultures, but from the same early G1 elutriated cells at different points as they progressed in the cell cycle (see *Materials and Methods*). The sum of all ribosomal protein abundances in assembled ribosomes did not change significantly in the cell cycle (Figure 4B). Since our samples were prepared from the same number of cells, and ribosomal proteins accounted for ~60% of the intensities detected, one could reasonably assume that ribosome abundance does not change significantly in the cell cycle, but it is also possible that our isolation somehow has skewed the results. There were also no significant differences in the relative abundance of the individual ribosomal proteins in the cell cycle (Figure 4C and Supplemental S7). We note that the relative levels of each protein in the ribosomes of each sample are independent of
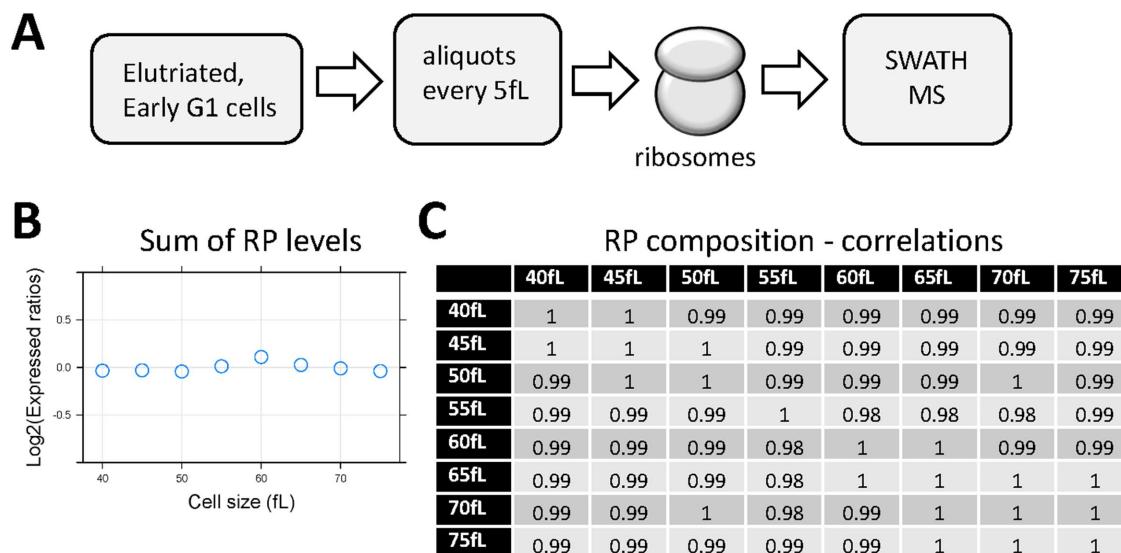
FIGURE 4: Ribosomal protein abundance in ribosomes does not change in the cell cycle. (A) Elutriated, early G1 cells were cultured, and sampled at regular intervals in the cell cycle, in three biological replicates at each 5 fL range, from 40 to 75 fL. Protein extracts from the same number of cells were then fractionated by sucrose ultracentrifugation, to isolate ribosomes on mRNAs, which were then analyzed by SWATH-MS (see *Materials and Methods*). (B) The peak areas corresponding to each ribosomal protein (RP) detected were summed and averaged across the triplicate for each cell size interval. The Log2(expressed ratios) values for the Sum of RP levels are shown on the *y*-axis, while cell size is on the *x*-axis. (C) Correlation matrix of the relative abundance of individual ribosomal proteins in assembled ribosomes on mRNAs. The Spearman correlation coefficients (ρ) shown in each case were calculated with the rcorr function of the *Hmisc* R language package. The cell cycle profiles for each ribosomal protein are shown in Supplemental Figure S7.

any putative differences in the amounts of assembled ribosomes between samples. Hence, we conclude that gross ribosome composition is the same during the cell cycle. These results do not support, but also do not unambiguously exclude, the possibility that individual, specialized ribosomes may be formed during the cell cycle. However, at least based on these population-averaged measurements, the composition of assembled ribosomes seems unaffected in the cell cycle.

Last, we interrogated our proteomic data for evidence of differences in codon usage during the cell cycle. It has been proposed that optimal codon usage is more prevalent in mRNAs expressed in the G1 phase of the cell cycle, contributing to the abundance of proteins that peak in G1 (Frenkel-Morgenstern *et al.*, 2012). Altered tRNA abundances during stress conditions in *S. cerevisiae* may also regulate protein synthesis (Torrent *et al.*, 2018). To avoid confounding effects from differential transcription of RNAs encoding the proteins that we identified to change in abundance in the cell cycle (Figure 3B), we focused on the proteins whose corresponding mRNAs were not changing in the cell cycle (Figure 2). Moreover, to minimize effects from regulated proteolysis, we excluded from the analysis proteins for which there is evidence for ubiquitylation and regulated proteolysis (Swaney *et al.*, 2013). For the vast majority of codons in the remaining proteins, there were no significant changes between their actual and expected frequencies in the cell cycle, based on gene-specific codon usage (Tumu *et al.*, 2012). Only four codons (AGC, UAU, AGG, AAC) were used with statistically significant differences in the cell cycle, but the magnitude of those differences was minimal nonetheless (Supplemental Figure S8). Overall, despite hints at the transcriptional level (Figure 2) for up-regulation of processes associated with protein synthesis in the G1 phase, at least from these population-based experiments, our data argue against any significant cell cycle-dependent changes in the ribosome content (Figure 4B and

Supplemental File S5), composition (Figure 4C), or codon usage (Supplemental Figure S8), suggesting that at the proteome level those changes in RNA levels have been dampened extensively.

Thiamine biosynthesis and thiamine diphosphate (TDP)-dependent enzymes in the cell cycle
To identify other proteins whose levels could change in the cell cycle but were not identified as such by the computational methods we used, we looked at proteins with the largest change in their levels, regardless of missing values or statistical cutoffs. Remarkably, a group of enzymes involved in thiamine biosynthesis peaked coordinately in abundance late in the cell cycle when the cells reached a cell size of ~65 fL (Figure 5A). These enzymes participate in TDP synthesis in the cytoplasm. Thi7p showed the smallest difference (slightly over twofold) in abundance during the cell cycle from our MS experiments and could provide a good measure to validate our results. The *THI7* transcript was not identified in the core cell cycle-regulated transcripts by Spellman *et al* (1998), which did not include in their analysis their own elutriation data. However, *THI7* was identified as cell cycle-regulated in all three elutriation datasets (this study, (Spellman *et al.*, 1998), (Blank *et al.*, 2017); and Supplemental Figure S3), suggesting that *THI7* expression is cell cycle-regulated at the RNA level, at least in experimental approaches that maintain the coordination of cell growth with cell division. To further test this prediction, early G1 cells carrying the *THI7-TAP* allele (the only available *THI* gene in the TAP-tagged strain collection encoding any of the proteins shown in Figure 5A) were obtained by elutriation, and the levels of the corresponding proteins were evaluated by immunoblotting at regular intervals as the cultures progressed in the cell cycle (Figure 5B). We confirmed by immunoblotting that the abundance of Thi7p was elevated late in the cell cycle (see Figure 5B, compared with the levels of the control protein Pgk1p). These results are
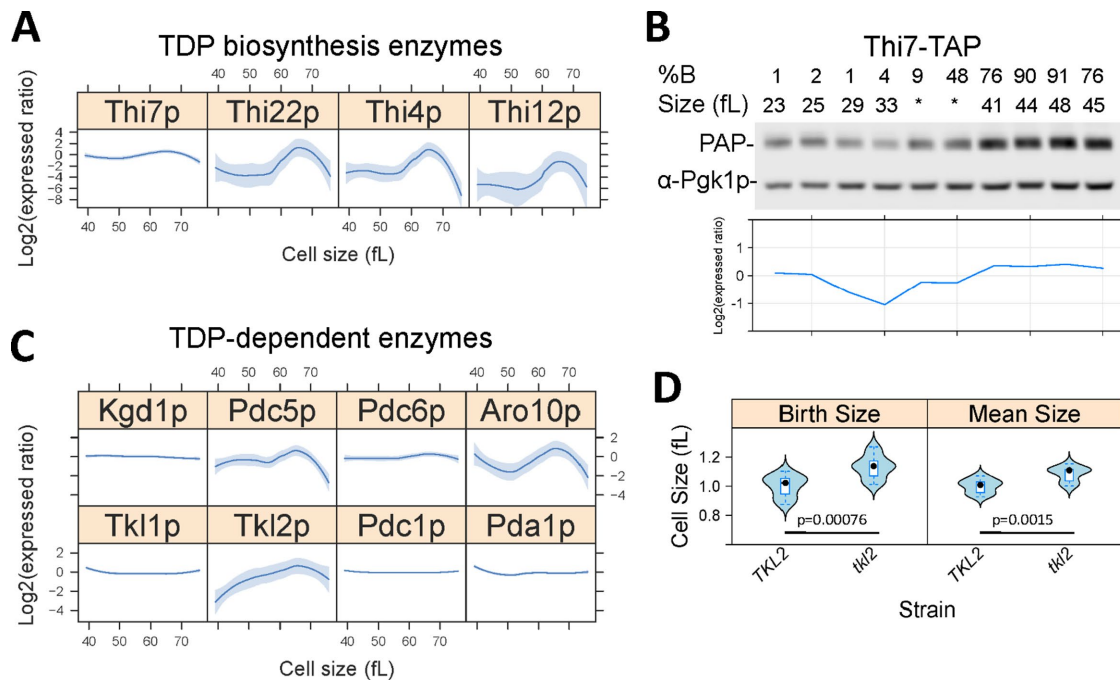
FIGURE 5: Thiamine biosynthesis and TDP-dependent enzymes in the cell cycle. (A) Abundances of the indicated proteins of thiamine biosynthesis from LC-MS/MS, across the cell size series (x-axis, in fL). The corresponding Log2(expressed ratios) values from all 24 data points are on the y-axis. Loess curves and confidence bands indicating the standard errors on the curve at a 0.95 level were drawn using the default settings of the panel.smoother function of the *latticeExtra* R language package. (B) The abundance of Thi7-TAP by immunoblotting from synchronous, elutriated cells, progressing in the cell cycle and sampled at regular intervals, as indicated (%B is the percentage of budded cells; fL is the cell size). Pgk1p levels are also shown from the same samples, to indicate loading. For the two samples indicated with an asterisk in the Thi7-TAP series, there were no size data due to instrument malfunction. At the bottom, the band intensities were quantified with ImageJ software, and the Log2-transformed expressed ratios of Thi7-TAP are shown, after they were normalized against Pgk1p. (C) Abundances of the indicated TDP-dependent proteins are determined and displayed as in A. (D) The birth and mean size of *tkl2* cells and experiment-matched wild-type (*TKL2*) cultures from exponentially dividing cells in rich, undefined medium (YPD). At least 12 independent cultures were measured in each case. Significant differences and the associated *p* values were indicated by the nonparametric Wilcoxon rank sum test, performed with the wilcox.test function of the R *stats* package.

consistent with the notion that there might be a coordinate, mitotic up-regulation of thiamine biosynthesis enzymes.

Next, we asked if any TDP-dependent enzymes also change in abundance in the cell cycle and if strains lacking these proteins have cell cycle-related phenotypes. TDP is a cofactor for several enzymes, including transketolase (Tkl1,2p), α-ketoglutarate dehydrogenase (Kgd1p), E1 subunit of pyruvate dehydrogenase (Pda1p), pyruvate decarboxylase (Pdc1,5,6p), and phenylpyruvate decarboxylase (Aro10p). Only the levels of Tkl2p, Pdc5p, and Aro10p appeared to be elevated late in the cell cycle (Figure 5C) at the same time as the levels of thiamine biosynthesis enzymes were also raised (Figure 5A).

Cell size phenotypes are often used as a proxy for disrupted cell cycle progression with an increased cell size phenotype typically accompanying mitotic defects. Of all deletion strains lacking a protein that requires TDP as a cofactor, only the loss of Tkl2p increased cell size significantly (Figure 5D). We found that both birth size and the mean size of *tkl2Δ* cells were larger (Figure 5D). Note that the *tkl2Δ* deletion strain was not in the panels that were examined in genomewide screens of cell size mutants (Jorgensen *et al.*, 2002; Zhang *et al.*, 2002). The mitotic up-regulation in the levels of thiamine biosynthesis enzymes (Figure 5A) and Tkl2p itself (Figure 5C) are suggestive of possible mitotic roles for Tkl2p, which might depend on the available TDP pools in the cell. In the

Discussion, we speculate on such putative roles based on the published reports.

Cell cycle-dependent changes in metabolites and lipids

From the same elutriated pools we used to measure RNAs and proteins (see Figure 1), we also measured metabolites and lipids. The assays were performed at the West Coast Metabolomics Center at University of California, Davis, a National Institutes of Health (NIH) Regional Comprehensive Metabolomics Resource Core. Each class of metabolites was measured with distinct MS-based assays (see *Materials and Methods*). From these assays, thousands of compounds were detected, but most could not be assigned confidently to known metabolites, and they were not considered further. Instead, we focused on the 406 primary metabolites, biogenic amines, and complex lipids that were identified across the cell size series. As with our analysis of RNAs and proteins, we used ANOVA (see Supplemental Table S1 and Figure 6) to identify compounds whose levels change in the cell cycle. Previous reports showed that storage carbohydrates are mobilized at the G1/S transition (Ewald *et al.*, 2016; Zhao *et al.*, 2016). In agreement with these studies, we also found that trehalose levels rise in G1 to their highest levels when cell size reaches 50 fL, but drop significantly at the G1/S transition (Figure 6). The levels of other sugars (glucose, fructose, mannose, and glucose-6-phosphate; see Figure 6) were also higher in G1,

Log2(expressed ratios)
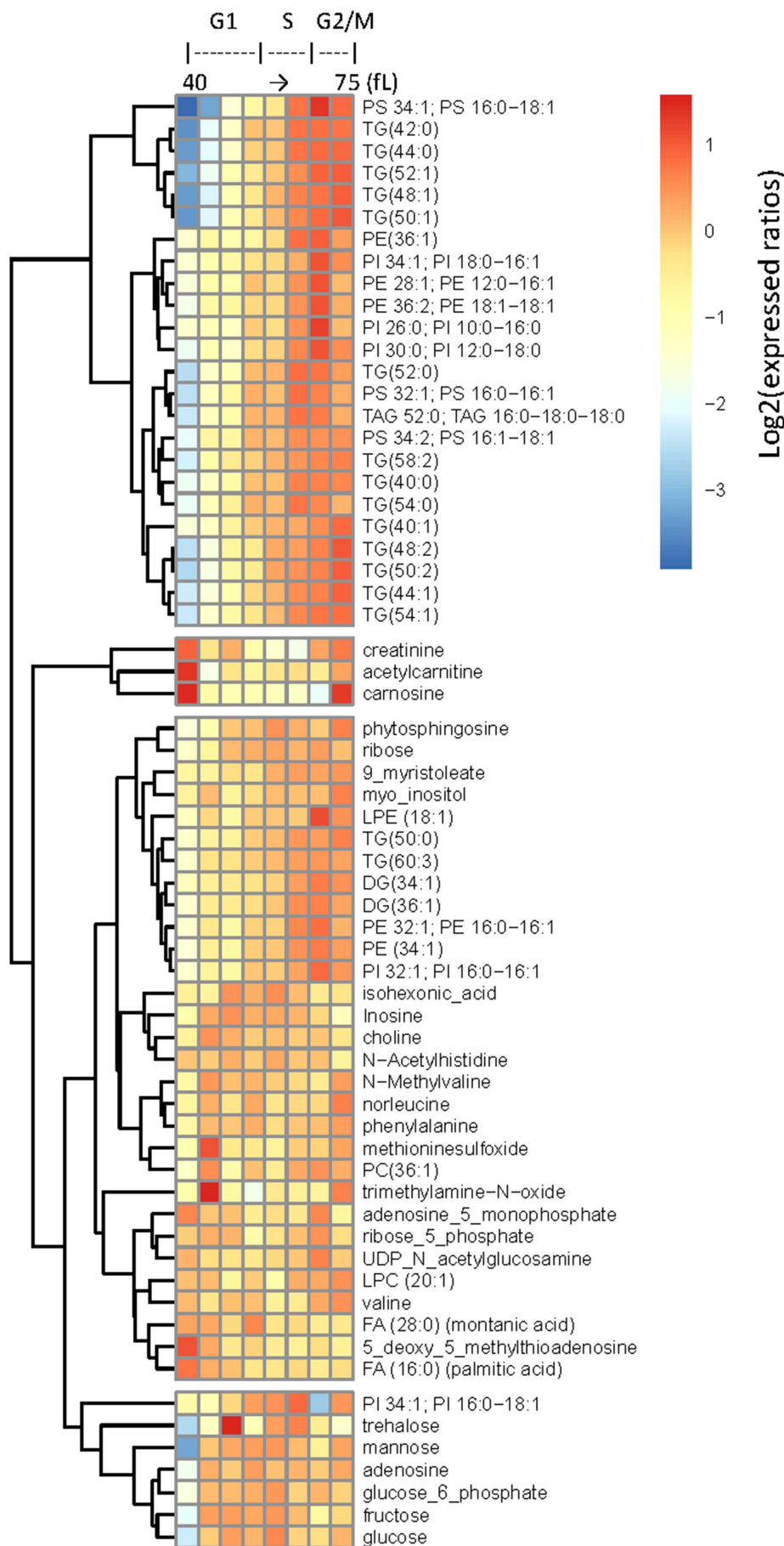
consistent with an up-regulation of glycolysis before DNA replication. By far, however, the class of metabolites that changed the most in abundance in the cell cycle was complex lipids, which peaked late in the cell cycle (Figure 6). These included phospholipids (phosphatidyl-inositol, -ethanolamine, and -serine) and triglycerides (Figure 6). The higher triglyceride levels are also consistent with the elevated levels of neutral lipid droplets late in the G2/M phase, as reported previously (Blank *et al.*, 2017). Overall, the coordinate increase in the levels of ergosterol biosynthesis enzymes we identified from the proteomic analysis (Figure 3A) and the increase in lipids (Figure 6) strongly suggest that lipid metabolism is significantly up-regulated late in the cell cycle. In the *Discussion*, we will expand on the significance of these results.

DISCUSSION

The sample-matched datasets for RNAs, proteins, metabolites, and lipids we generated from budding yeast cells progressing synchronously in the cell cycle provide a comprehensive view of these biomolecules in dividing cells. We discuss our approach to obtain the analytical samples and our findings in the context of the relation between the transcriptome and the proteome and the integration of metabolite and lipid measurements with other "omic" datasets.

A primary goal and unique aspect of this study are that we took a measure of the different biomolecules from the same, experiment-matched samples. Furthermore, to maintain the normal coupling between cell growth and cell division as much as possible, we used centrifugal elutriation to obtain synchronous cultures, instead of arrest-and-release methods. However, elutriation merely selects based on cell size

FIGURE 6: Lipid levels change significantly in the cell cycle. (A) From 406 known metabolites identified from all classes (primary, biogenic amines, complex lipids), the levels of 64 with significantly different levels ($p < 0.05$; Log2(FC) $\geq$ 1) between any two points in the cell cycle, based on bootstrap ANOVA, are shown in the heatmap. The levels of each metabolite were the average of each triplicate for the cell size indicated, which was then divided by the average value of the entire cell size series for that metabolite. These expressed ratios were then Log2-transformed. The Log2(expressed ratios) values were hierarchically clustered and displayed with the *pheatmap* R language package. The different columns of the heatmap correspond to the different cell sizes (40–75 fL, left to right, in 5-fL intervals).

a small fraction of cells from an asynchronous, larger population. Hence, compared with arrest-and-release methods, elutriation suffers from low yields of synchronous cells. To overcome this problem, we generated our samples by pooling from different elutriations cells of the same size. All the cells we collected from the elutriator were early G1 daughter cells, which were then allowed to progress in the cell cycle before we harvested them once they reached a particular cell size. We then used cell size as a metric to arrange these pools along a hypothetical cell cycle, generating a size series (Figure 1). This is different from starting with one elutriated sample, typically of small cells in early G1, and then taking aliquots at various times as they progress in the cell cycle, generating a time series.

But practical necessities for large quantities of cells aside, how does a size-based series compare to a time-based one? We argue that it compares favorably for the following reasons: first, no two, time series-based elutriations are the same, and cell size always has to be used to account for experimental variation properly. A typical metric is the critical size for START, defined as the size at which half the cells are budded. We note that the critical size of our reconstructed cell cycle profile was ~62 fL (Figure 1B), the same as the critical size of the same strain and medium in time-series experiments (Hoose *et al.*, 2012). Second, based on DNA content analysis (Supplemental Figure S1), at least until the cells have grown substantially to ~65 fL, the synchrony appears very tight. Only at 70–75 fL, the samples appear more heterogeneous, with some cells going through the M/G1 transition, indicated by the rise of cells with G1 DNA content. But this is also a feature of time-based elutriations, or even arrest-and-release methods, where there is an inevitable loss of synchrony the further one moves along the cell cycle from the starting point (Mitchison, 1971). Third, every molecular marker we looked at (cyclin mRNAs, see Figure 1C; proteins of DNA metabolism, see Figure 3A) peaks as expected in our size-based series. Fourth, when comparing the cell cycle abundances of the same protein (Thi7p) from a size-based (Figure 5A) versus a time-based series (Figure 5B), the profiles are nearly identical, even though the ploidy of the strains was not. For these reasons, our size-based approach recapitulates the expected properties of synchronous, elutriated samples.

In yeast, the latest meta-analyses from all available studies estimated that between 37 and 56% of the variance in protein abundance is explained by mRNA abundance (Ho *et al.*, 2018). These estimates are within the range of previous ones from multiple species (Vogel and Marcotte, 2012). Based on the absolute quantification of protein and mRNA abundances (Lahtvee *et al.*, 2017), the overall correlation between mRNA and protein abundances was also in that range (R^2 = 0.45, based on Pearson's correlation coefficient). The level of correlation between the transcriptome and the proteome we observed appears to be somewhat higher (ρ = 0.52–0.63, based on Spearman's coefficient), probably because our experiments were done from synchronous cells, and because cell cycle transitions are associated with transcriptional waves (Spellman *et al.*, 1998). A critical role for transcription in shaping the proteome takes place as cells transition in different environments, and during such transitions changes in protein levels were much more highly correlated with the changes in mRNA levels (R^2 > 0.9) (Lahtvee *et al.*, 2017). Hence, the relatively high correlation we observed between the transcriptome and the proteome in the cell cycle is not surprising, and it is probably an underestimate, since some extremely unstable cell cycle regulators whose levels rise as a result of transcription (e.g., cyclins, see Figure 1C) were absent from our proteomic datasets because of their low abundance.

Despite the correlation between the transcriptome and the proteome we discussed above, there were clear groups of transcripts and proteins whose abundance was incongruent. Ribosomal biosynthesis, reflected on the levels of individual ribosomal proteins or assembled ribosomes, was not periodic at the proteomic level (Figure 4 and Supplemental Figure S7), despite a large G1 transcriptional wave of RNAs involved in this process (Figure 2). We noted that a similar phenomenon was recently reported for the integrated stress response, a well-characterized transcriptional response in yeast involving ~900 transcripts (Gasch *et al.*, 2000), which was not seen at all at the protein level (Ho *et al.*, 2018). The observation that the ribosome content of the cell is constant in the cell cycle (Figure 4) suggests that changes in translational efficiency of some mRNAs described previously (Blank *et al.*, 2017) are likely due to transcript-specific mechanisms, rather than global changes in the steady-state ribosome content (Lodish, 1974).

The mitotic peak in the levels of TDP biosynthesis enzymes was surprising (Figure 5). The physiological significance of such a change in the levels of these enzymes is unclear. Through some uncharacterized roles, the TDP-dependent transketolase activity is necessary for meiotic progression in mouse oocytes (Kim *et al.*, 2012). In bacteria, transketolase participates in chromosomal topology, and *Escherichia coli* cells lacking transketolase are UV sensitive (Hardy and Cozzarelli, 2005). However, we found that yeast *tkl2Δ* cells are not sensitive to UV or other DNA-damaging agents (not shown). Overall, despite the intriguing observations that late in the cell cycle, levels of the TDP-dependent Tkl2p transketolase were higher (Figure 5C) and loss of Tkl2p increased cell size (Figure 5D), the molecular mechanism connecting these observations remains to be determined.

The coordinate up-regulation of ergosterol biosynthetic enzymes late in the yeast cell cycle (Figure 3), not evident at the RNA level (Figure 2), was unexpected. To our knowledge, there is no prior report of such a response. It should be noted that the lack of cell cycle-dependent changes at the levels of mRNAs encoding the enzymes of ergosterol biosynthetis was seen not only in our dataset but also in the other datasets aggregated in the Cyclebase 3.0 database for yeast and other organisms (Santos *et al.*, 2015). Of the enzymes we show in Figure 3A, only *ERG3* had a rank score of 624, while all others were not periodic (scores > 800) (Santos *et al.*, 2015). Note that we also found *ERG3* mRNA levels to significantly change in the cell cycle (see Supplemental File S4/Sheet: rnas_anova_heatmap).

The mitotic rise in the levels of sterol biosynthetic enzymes is significant in the context of our metabolite measurements, showing that lipid levels (especially phospholipids and triglycerides) increased at the same time (Figure 6). Our observations are consistent with several other reports linking lipid metabolism with cell cycle progression and mitotic entry in yeast (Anastasia *et al.*, 2012; McCusker and Kellogg, 2012). Levels of triglycerides increase in wild type cells synchronized in mitosis (Blank *et al.*, 2017), storage of triglycerides in lipid droplets is thought to fuel mitotic exit (Yang *et al.*, 2016), and lipid-exchange proteins integrate lipid signaling with cell cycle progression (Huang *et al.*, 2018). Note that there have not been analytical measurements of distinct lipids in the cell cycle in yeast. The data we show here are not only consistent with but also significantly expand the prior studies mentioned above. It is also important to stress that an increase in lipids late in the cell cycle cannot simply be due to a need for cell surface material. We had shown previously that increased lipogenesis does not increase cell size (Blank *et al.*, 2017). Hence, the increase in the abundance of lipids likely

reflects changes in the composition of membranes or other more specialized, cell cycle-dependent process, not necessarily a simplistic need for more cell surface building blocks.

One also needs to consider the dramatic changes in cellular morphology. Especially during mitosis, when the cell adopts the characteristic hourglass structure. The lipid content must accommodate dynamic changes in membrane curvature. For example, during cytokinesis, it is thought that lipids that confer negative curvature must be deposited on the outer leaflet of the bilayer (Furse and Shearman, 2018). In yeast and human cells, inhibition of de novo fatty acid biosynthesis arrests cells in mitosis (Hasslacher et al., 1993; Schneiter et al., 1996; Al-Feel et al., 2003; Scaglia et al., 2014). In human cells, cholesterol synthesis may affect multiple points in the cell cycle. In an earlier report, inhibition of cholesterol synthesis arrested human cells in mitosis (Suarez et al., 2002), while in a later report the cells arrested in G1 (Singh et al., 2013). Cholesterol's role in mitosis appears to be complex, not only affecting the distribution of phospholipids in the plasma membrane but also governing the formation of a vesicular network at the midbody during cytokinesis (Kettle et al., 2015). Interestingly, ergosterol may have a cell cycle regulatory role in yeast, distinct from its bulk, structural role in membrane integrity (Dahl et al., 1987), but that role remains unclear (Gaber et al., 1989).

Last, our results argue for posttranscriptional mechanisms leading to mitotic up-regulation of sterol biosynthesis. As to how the differential abundance of the ergosterol biosynthetic enzymes might come about, we note that all the enzymes we show in Figure 3A, including Erg3p, have been shown to be ubiquitinylated (Peng et al., 2003; Swaney et al., 2013), raising the possibility of regulated proteolysis. Another possibility is translational control. In our previous analysis of translational control in the cell cycle by ribosome profiling, a confounding problem was the poor overlap of the different computational pipelines we used to analyze the data (Aramayo and Polymenis, 2017; Blank et al., 2017). Proteomic data provide an independent metric that allows us to revisit the datasets of translationally controlled transcripts in the cell cycle. We found that for 38 transcripts (from Dataset 5 in Blank et al., 2017) identified by the babel pipeline (Olshen et al., 2013) and 45 transcripts (from Dataset 7 in Blank et al., 2017) identified by the anota pipeline (Larsson et al., 2011), the corresponding protein levels are indeed significantly periodic in the cell cycle (Supplemental File S4/Sheet: proteins_anova_heatmap). These results (see Supplemental File S9) validate the translational control of transcripts we had not followed up, but were identified by both computational approaches (e.g., NQM1, MSC1, with the protein levels peaking as predicted late in the cell cycle) and point to new ones, ERG5 among them. Hence, multiple levels of control, such as transcription (for ERG3), translation (for ERG5), and protein degradation (possibly for all Erg proteins) may contribute to the mitotic up-regulation of ergosterol biosynthesis. Furthermore, integrating our proteomic and ribosome profiling datasets increased the confidence for fivefold more transcripts that are likely under translational control in the cell cycle, providing an example of the synergy among different studies and datasets.

Our data also underscore the value of having metabolite measurements along with other omic datasets to strengthen the efforts of identifying physiologically relevant cellular responses. In future work, employing targeted metabolic profiling and flux analysis in the cell cycle will increase our understanding of how the transcriptome and proteome shape dynamic changes in metabolism and how resources are allocated during cell division.

MATERIALS AND METHODS

See Table 1 for reagents and tools. Where known, the Research Resource Identifiers (RRIDs) are shown.

Strains and media

All the strains used in this study are shown in the Table 1. Unless noted otherwise, the cells were cultivated in the standard, rich, undefined medium YPD (1%$^{wt/vol}$ yeast extract, 2%$^{wt/vol}$ peptone, 2%$^{wt/vol}$ dextrose) at 30°C (Kaiser et al., 1994).

Elutriation

To collect enough cells for the downstream measurements of RNA, proteins, and metabolites, we followed the same strategy we described previously (Blank et al., 2017). Briefly, elutriated wild-type, G1 cells (diploid BY4743 background) were allowed to progress in the cell cycle until they reached the desired cell size. At that point, they were quenched (with 100 μg/ml cycloheximide and 0.1% sodium azide), frozen away, and later pooled with cells of similar size (Figure 1A). Overall, we had to collect 101 individual samples to generate the 24 pools shown in Figure 1A.

For other elutriation experiments (e.g., see Figures 4 and 5), only an early G1 elutriated fraction was collected, from which samples were taken at regular intervals as the cells progressed in the cell cycle.

Cell size and DNA content measurements

The methods to measure DNA content and the cell size (birth or mean size) of asynchronous cultures and estimate the critical size of asynchronous cultures have been described in detail previously (Guo et al., 2004; Truong et al., 2013; Soma et al., 2014; Maitra et al., 2019).

Proteomic samples

We used ~1E+09 cells from each of the 24 pools of the cell size series (see Figure 1) to prepare extracts for LC-MS/MS. For each sample, the cells were resuspended in 0.75 ml of lysis solution (10 mM Tris, pH 7.8, 10 mM NaCl). Glass beads were added to the top of liquid level, the samples were placed in a Mini Beadbeater (Biospec), and the cells were broken by "bead-beating" twice at the maximum speed for 90 s each time, placed on ice for 60 s between. The extract from each sample was collected by punching a hole with a 21-gauge syringe needle at the bottom of the tube. Last, the soluble material from the lysates were clarified by centrifugation at $14,000 \times g$ at 4°C for 10 min. Insoluble pellets were resuspended in 500 μl of lysis buffer and both clarified supernatants and pellets were stored at –80°C until processing for MS.

For mass spectral analysis, clarified extracts were thawed and protease inhibitors were immediately added. Each supernatant sample (50 μl) was mixed with 50 μl trifluoroethanol (TFE) and reduced with 5 mM tris(2-carboxyethyl)phosphine (TCEP) at 56°C for 45 min, cooled for 5 min at room temperature, and alkylated with 25 mM iodoacetamide in the dark at room temperature for 30 min. Samples were diluted 10-fold with digestion buffer (50 mM Tris, pH 8.0, 2 mM calcium chloride) and digested with trypsin (added at 1:50 ratio) at 37°C for 5 h. Digestion was stopped with 100 μl of 10% formic acid and sample volumes were reduced to 100–250 μl in a SpeedVac. Following filtration with an Amicon Ultra-15 Centrifugal Filter Unit, the peptides were desalted using C18 Spin Tips, according to the manufacturer's instructions. The volume of the samples was then reduced to 5–10 μl in a SpeedVac. Last, the samples were resuspended in 100 μl of a 95% water, 5% acetonitrile, 0.1% formic acid solution and subjected to LC-MS/MS analysis.

Designation	Source	Identifier/Catalog#		Additional information
S. cerevisiae strain	(Giaever *et al.*, 2002); http://www.euroscarf.de/index.php?name= News	RRID:SCR_003093	BY4743	*MATa/α his3Δ1/his3Δ1 leu2Δ0/leu2Δ0 LYS2/lys2Δ0 met15Δ0/MET15 ura3Δ0/ura3Δ0*
S. cerevisiae strain	(Giaever *et al.*, 2002); http://www.euroscarf.de/index.php?name= News	RRID:SCR_003093	BY4742	*MATα his3Δ1 leu2Δ0 lys2Δ0 ura3Δ0*
S. cerevisiae strain	(Giaever *et al.*, 2002); http://www.euroscarf.de/index.php?name= News	RRID:SCR_003093	BY4741	*MATa his3Δ1 leu2Δ0 met15Δ0 ura3Δ0*
S. cerevisiae strain	Dharmacon	YSC1178-202232418		*THI7-TAP::HIS3MX6*, BY4741 otherwise
S. cerevisiae strain	Dharmacon	YSC6272-201919629	13256	*tkl2Δ::KanMX*, BY4742 otherwise
Chemical, reagent	Sigma-Aldrich	Y1625		Yeast extract
Chemical, reagent	Sigma-Aldrich	P5905		Peptone
Chemical, reagent	Sigma-Aldrich	D9434		Dextrose
Chemical, reagent	Calbiochem	239763-M		Cycloheximide
Chemical, reagent	Sigma-Aldrich	S2002		Sodium azide
Chemical, reagent	Sigma-Aldrich	252859		Tris(hydroxymethyl)aminomethane
Chemical, reagent	Roche	TRIS-RO		Tris base
Chemical, reagent	Sigma-Aldrich	S7653		Sodium chloride
Chemical, reagent	Sigma-Aldrich	792780		Ethanol
Chemical, reagent	Sigma-Aldrich	S2889		Sodium acetate
Chemical, reagent	Sigma-Aldrich	D5758		DEPC
Chemical, reagent	Ambion	AM9720		Acid-phenol:chloroform, pH 4.5 (with IAA, 125:24:1)
Chemical, reagent	USP	1374248		Magnesium chloride hexahydrate
Chemical, reagent	Sigma-Aldrich	D0632		DTT
Chemical, reagent	Sigma-Aldrich	T8787		Triton X-100
Chemical, reagent	ThermoFisher	AM2238		Turbo DNase I
Chemical, reagent	Scientific Industries	SI-BG05		Glass beads
Consumable	Beckman Coulter	349622		13×51 mm polycarbonate centrifuge tubes
Chemical, reagent	Sigma-Aldrich	S0389		Sucrose
Chemical, reagent	Sigma-Aldrich	P4417		PBS
Chemical, reagent	ThermoFisher Scientific	84850		C18 Spin Tips
Chemical, reagent	Millipore	Z720003		C18 Ziptips
Chemical, reagent	Sigma-Aldrich	436143		SDS
Chemical, reagent	Sigma-Aldrich	207861		Ammonium carbonate
Chemical, reagent	Sigma-Aldrich	650501		Acetone
Chemical, reagent	Sigma-Aldrich	D6750		Sodium deoxycholate
Chemical, reagent	ThermoFisher Scientific	77720		TCEP, Bond-Breaker TCEP Solution
Chemical, reagent	Sigma-Aldrich	I6125		Iodoacetamide
Chemical, reagent	Pierce	90058		Trypsin protease, MS-grade
Chemical, reagent	Sigma-Aldrich	F0507		Formic acid
Chemical, reagent	Sigma-Aldrich	C7715		Amicon Ultra-15 Centrifugal Filter Units
Chemical, reagent	Sigma-Aldrich	499609		Calcium chloride
Chemical, reagent	Sigma-Aldrich	T63002		TFE
Chemical, reagent	Sigma-Aldrich	H3375		4-(2-Hydroxyethyl)piperazine-1-ethanesulfonic acid, N-(2-Hydroxyethyl)piperazine-N'-(2-ethanesulfonic acid) (HEPES)

TABLE 1: Reagents and tools.

(Continues)

Designation	Source	Identifier/Catalog#	Additional information
Chemical, reagent	Sigma-Aldrich	78830	Phenylmethanesulfonyl fluoride
Chemical, reagent	Sigma-Aldrich	431788	EDTA
Chemical, reagent	ThermoFisher	D1306	4',6-Diamidino-2-Phenylindole, Dihydrochloride
Chemical, reagent	Epicentre	MRZY1324	Ribo-Zero Magnetic Gold Kit (Yeast), for rRNA sub-traction
Chemical, reagent	Epicentre	SSV21124	SciptSeq v2 RNA-Seq Library Preparation Kit
Antibody	Sigma-Aldrich	P1291	PAP soluble complex
Antibody	abcam	ab38007	Anti-Pgk1p antibody, rabbit polyclonal
Chemical, reagent	ThermoFisher	XP04125	Novex WedgeWell 4-12% Tris-Glycine gels
Software, algorithm	https://www.metaboanalyst.ca/	RRID:SCR_015539	MetaboAnalyst, web server for statistical, functional and integrative analysis of metabolomics data
Software, algorithm	Beckman Coulter	383550	AccuComp Z2, software to monitor number and size of cells with Z2 cell counter
Software, algorithm	https://www.nikoninstruments.com/Products/Software	RRID:SCR_014329	NIS-Elements, microscope imaging software suite used with Nikon products
Software, algorithm	https://imagej.net/	RRID:SCR_003070	ImageJ, image processing software
Software, algorithm	http://www.rstudio.com/	RRID:SCR_000432	RStudio, software for the R statistical computing environment
Software, algorithm	http://www.yeastgenome.org/	RRID:SCR_004694	SGD, Saccharomyces Genome Database
Software, algorithm	https://www.r-project.org	v3.5.2 RRID:SCR_001905	R, Statistical Computing Environment
Software, algorithm	http://www.geneontology.org/	RRID:SCR_002811	Gene ontology, enrichment analysis
Software, algorithm	https://biognosys.com/shop/spectronaut		Spectronaut, Biognosys software for the targeted analysis of DIA measurements from various MS platforms

TABLE 1: Reagents and tools. Continued.

The insoluble pellets from the same extracts described above were processed based on a method reported previously (Lin *et al.*, 2013). The pellets were resuspended in 50 µl of 2%$^{wt/vol}$ SDS, 50 mM ammonium carbonate and heated at 95°C for 10 min. Following clarification, each supernatant was transferred to a fresh tube, mixed with 6 vol of cold acetone (–20°C), and incubated at 4°C for 4 h to form a precipitate. Precipitate was recovered by centrifugation at 13,000 × *g* for 15 min, the supernatant was carefully removed by aspiration, and the pellets were washed twice with 0.4 ml of cold acetone. After each wash, the samples were centrifuged at 14,000 × *g* for 1 min and the supernatant was carefully aspirated. Pellets were solubilized in 500 µl of 1% wt/vol sodium deoxycholate, 50 mM ammonium carbonate with two rounds of sonication (10 min each) in a water bath sonicator with 5 min on ice in between. Each sample (50 µl) was reduced and alkylated with TCEP and iodoacetamide as described above. Unreacted iodoacetamide was quenched with 12 mM dithiothreitol (DTT). The samples were brought to 80 µl with digestion buffer and digested with trypsin (added at 1:50 ratio) at 37°C for 5 h. Digestion was stopped with 1% formic acid and samples were centrifuged at 14,000 × *g* for 10 min to pellet the precipitated sodium deoxycholate. Peptides were desalted with C18 Spin Tips and resuspended for LC-MS/MS as described above.

LC-MS/MS

Mass spectra were acquired on a Thermo Orbitrap Fusion. Supernatant samples (5 µl) or pellet samples (2 µl) of peptides were separated using reverse phase chromatography on a Dionex Ultimate 3000 RSLCnano UHPLC system (Thermo Fisher Scientific) with a C18 trap to Acclaim C18 PepMap RSLC column (Dionex; Thermo Fisher Scientific) configuration. Peptides were eluted using a 3–45% acetonitrile gradient over 70 min and directly injected into the mass spectrometer using nano-electrospray. Data-dependent tandem MS was performed using a top speed high-energy collision-induced dissociation (HCD) method with full precursor ion scans (MS1) collected at 120,000 m/z resolution and a cycle time of 3 s. Monoisotopic precursor selection and charge-state screening were enabled, with ions of charge > +1 selected with dynamic exclusion of 30 s for ions selected once within a 30-s window. Selected precursor ions underwent HCD at 31% energy stepped ±4%. All MS2 scans were centroid and done in rapid mode. Raw files were processed using Proteome Discoverer 2.2 and the label-free quantification workflow.

RNA samples and libraries

We used the same approach we had described previously (Blank *et al.*, 2017) to collect cells from elutriated cultures of wild type

(BY4743 strain background). For each of the 24 samples, from ~3E+07 cells total RNA was prepared with the hot phenol method. Briefly, the frozen pellets were resuspended in 0.4 ml TES buffer (10 mM Tris, pH = 7.5, 10 mM EDTA, 0.5% SDS), in Diethyl pyrocarbonate (DEPC)-treated water, and ~0.05-ml glass beads were added. Then, 0.4 ml of acid phenol:chloroform was added to each pellet, and the samples were incubated at 65°C for 30 min and vortexed briefly every 5 min during that time. The samples were centrifuged at 14,000 × g for 5 min, and 0.3 ml of the top, aqueous layer were placed in a 2-ml screw-cap tube containing 1 ml cold ethanol with 40 μl of a 3M sodium acetate solution. The samples were incubated at 4°C overnight and then centrifuged at 14,000 × g for 20 min. The pellets were washed with 80% ethanol and centrifuged at 14,000 × g for 5 min. The pellets were air-dried and resuspended in 25 μl of DEPC-treated water. For the RNAseq libraries, we also used the same approach we had described (Blank et al., 2017), except that we did not select for polyA-tailed RNAs. Instead, from total RNA, we depleted rRNA using the Ribo-Zero Magnetic Gold Kit (Yeast) according to the manufacturer's instructions. All libraries were sequenced on an Illumina HiSeq4000, with multiplexing, at the Texas A&M AgriLife Genomics and Bioinformatics Facility. Raw sequencing data (fastq files) have been deposited (GEO: GSE135476).

The reads were aligned to the *S. cerevisiae* reference genome (version R64-1-1) using the *Rsubread* R language package (Liao et al., 2019). First, an index was built using the command: buildindex(basename = "R64", reference = "Saccharomyces_cerevisiae.R64-1-1.dna.toplevel.fa", gappedIndex = TRUE). Then, for each of the 24 libraries, the paired-end reads were aligned with the command: align(index = 'R64', readfile1 = '….fastq.gz', readfile2 = '….fastq.gz', type = "rna"). For each library, we obtained > 10 million uniquely mapped reads, and the output BAM files were then used in the featureCounts function of the *Rsubread* package, with the following command: featureCounts(files = "…subread.BAM", ispairedEnd = TRUE, requireBothEndsMapped = TRUE, annotext = "Saccharomyces_cerevisiae.R64-1-1.95.gtf", countChimericFragments = FALSE, isGTFAnnotationFile = TRUE). All the read counts are in Supplemental File S1/Sheet: "rna_reads."

For differential RNA levels between any two points in the cell cycle using the *DESeq2* R language package (Love et al., 2014), the raw read data (Supplemental File S2/Sheet: rna_deseq2_i) were used as input. For this statistical analysis, the 24 cell size pools were grouped in eight groups for each of the ~ 5-fL increments in the cell size series (see Figure 1A). Additional analyses with ANOVA-based methods were performed as for the other biomolecules, and they are described below.

Metabolite samples and analysis
The untargeted, primary metabolite, biogenic amine, and complex lipid analyses were done at the NIH-funded West Coast Metabolomics Center at the University of California at Davis, according to their MS protocols. GC-TOF MS was used for Primary metabolites. For biogenic amines, separation and detections was achieved by HILIC, followed by Quadrupole time-of-flight (QTOF) MS/MS. Last, for complex lipids, CSH C18 separation was followed with QTOF MS/MS for lipids. Extract preparation was also done at the same facility from 1E+07 cells in each sample from the same ones used for proteomic and RNA profiling (Figure 1). The cells were provided to the Metabolomics facility as frozen (at –80°C) pellets. Detected species that could not be assigned to any compound were excluded from the analysis.

ANOVA-based computational approaches to identify differentially expressed biomolecules
For RNA samples, we used the TPM normalized values. For all other biomolecules, the input values we used were scale-normalized for input values per sample. All the input and output datasets are shown in Supplemental Table S1. To identify significant differences in the levels of biomolecules between any two points in the cell cycle we used the robust bootstrap ANOVA, via the *t1waybt* function, and the posthoc tests via the *mcppb20* function, of the *WRS2* R language package (Wilcox, 2011). The function is shown in Supplemental File S6, using as an example the Supplemental File S2/sol_pa_anova spreadsheet. For this statistical analysis, the 24 cell size pools were grouped in eight groups for each of the ~5-fL increments in the cell size series (see Figure 1A).

SWATH-MS
The samples used to measure ribosomal protein abundances were from elutriated, diploid wild-type BY4743 cells (see Table 1). Once the cells reached the desired cell size, they were quenched with 100 μg/ml cycloheximide and 0.1% sodium azide. Cells were harvested from three independently elutriated cultures (5E+07 cells in each sample). The cells were resuspended in a buffer containing 20 mM Tris·Cl (pH 7.4), 150 mM NaCl, 5 mM MgCl$_2$, 1 mM DTT, 100 μg/ml cycloheximide, 1% $^{vol/vol}$ Triton X-100, and 25 U/ml Turbo DNase I to a volume of 0.35 ml. Then, 0.2 ml of 0.5-mm glass beads were added to each sample and vortexed at maximum speed for 15 s eight times, placing on ice for 15 s in between. The lysates were clarified by centrifuging at 5000 rpm for 5 min at 4°C and again for 5 min at 13,000 rpm at 4°C. The supernatant was transferred to a 13 × 51 mm polycarbonate ultracentrifuge tube and underlaid with 0.90 ml of 1 M sucrose, and the ribosomes were pelleted by centrifugation in a TLA100.3 rotor (Beckman) at 100,000 rpm at 4°C for 1 h. The protein pellets from three biological replicates for various time points during the cell cycle (40, 45, 50, 55, 60, 65, 70, and 75 fL) were then resuspended in phosphate-buffered saline (PBS), subjected to a Filter-Aided Sample Preparation protocol tryptic digestion (Wisniewski et al., 2009), desalted using C-18 Ziptips, and analyzed by data-independent acquisition (DIA)/SWATH-MS, as described previously (Schilling et al., 2017).

Briefly, samples were analyzed by reverse-phase HPLC-ESI-MS/MS using an Eksigent Ultra Plus nano-LC 2D HPLC system (Dublin, CA) with a cHiPLC system (Eksigent), which was directly connected to a quadrupole time-of-flight (QqTOF) TripleTOF 6600 mass spectrometer (SCIEX, Concord, Canada) (Christensen et al., 2018). After injection, peptide mixtures were loaded onto a C18 precolumn chip (200 μm × 0.4 mm ChromXP C18-CL chip, 3 μm, 120 Å, SCIEX) and washed at 2 μl/min for 10 min with the loading solvent (H$_2$O/0.1% formic acid) for desalting. Subsequently, peptides were transferred to the 75 μm × 15 cm ChromXP C18-CL chip, 3 μm, 120 Å, (SCIEX) and eluted at a flow rate of 300 nl/min with a 3 h gradient using aqueous and acetonitrile solvent buffers.

For quantification, all peptide samples were analyzed by data-independent acquisition (Gillet et al., 2012), using 64 variable-width isolation windows (Collins et al., 2017; Schilling et al., 2017). The variable window width is adjusted according to the complexity of the typical MS1 ion current observed within a certain m/z range using a DIA "variable window method" algorithm (more narrow windows were chosen in "busy" m/z ranges, wide windows in m/z ranges with few eluting precursor ions). DIA acquisitions produce complex MS/MS spectra, which are a composite of all the analytes

within each selected Q1 m/z window. The DIA cycle time of 3.2 s included a 250-ms precursor ion scan followed by 45 ms accumulation time for each of the 64 variable SWATH segments.

The DIA/SWATH data was processed with the Spectronaut software platform (Biognosys) for relative quantification comparing peptide peak areas among different time points during the cell cycle. For the DIA/SWATH MS2 data sets, quantification was based on XICs of 6-10 MS/MS fragment ions, typically y- and b-ions, matching to specific peptides present in the spectral libraries. Significantly changed proteins were accepted at a 5% FDR (q value < 0.05).

Immunoblot analysis

For protein surveillance, protein extracts were made as described previously (Amberg *et al.*, 2006) and run on 4–12% Tris-Glycine SDS–PAGE gels. To detect TAP-tagged proteins with the Peroxidase Anti-Peroxidase (PAP) reagent, we used immunoblots from extracts of the indicated strains as we described previously (Blank *et al.*, 2017). Loading was evaluated with an anti-Pgk1p antibody.

Comparison of the relative protein abundances in Becher *et al.* (2018) and Olsen *et al.* (2010)

For the datasets generated in human HeLa cells 0.5 h after nocodazole arrest, the data were from Table S3 in Becher *et al.* (2018) and Supplemental Table_S1 in Olsen *et al.* (2010). In the former study, the authors reported the Log2-transformed ratios of the measured abundance over the median abundance of asynchronous cultures. For the Olsen *et al.* (2010) proteins, the data were the isotopic ratios reported. In both cases, these values represented the corresponding protein abundances in that sample among all the proteins identified in each sample in each study. To compare the rank order of the 3243 proteins identified in common in the two studies, the Spearman's rank correlation rho (ρ) was estimated ($\rho = 0.245$).

REFERENCES

Ahn E, Kumar P, Mukha D, Tzur A, Shlomi T (2017). Temporal fluxomics reveals oscillations in TCA cycle flux throughout the mammalian cell cycle. Mol Syst Biol 13, 953.

Al-Feel W, DeMar JC, Wakil SJ (2003). A Saccharomyces cerevisiae mutant strain defective in acetyl-CoA carboxylase arrests at the G2/M phase of the cell cycle. Proc Natl Acad Sci USA 100, 3095–3100.

Amberg DC, Burke DJ, Strathern JN (2006). Yeast protein extracts. CSH Protoc 2006, pdb. prot4152.

Anastasia SD, Nguyen DL, Thai V, Meloy M, MacDonough T, Kellogg DR (2012). A link between mitotic entry and membrane growth suggests a novel model for cell size control. J Cell Biol 197, 89–104.

Aramayo R, Polymenis M (2017). Ribosome profiling the cell cycle: lessons and challenges. Curr Genet 63, 959–964.

Atilla-Gokcumen GE, Muro E, Relat-Goberna J, Sasse S, Bedigian A, Coughlin ML, Garcia-Manyes S, Eggert US (2014). Dividing cells regulate their lipid composition and localization. Cell 156, 428–439.

Banfalvi G (2008). Cell cycle synchronization of animal cells and nuclei by centrifugal elutriation. Nat Protoc 3, 663–673.

Becher I, Andres-Pons A, Romanov N, Stein F, Schramm M, Baudin F, Helm D, Kurzawa N, Mateus A, Mackmull MT, et al. (2018). Pervasive protein thermal stability variation during the cell cycle. Cell 173, 1495–1507.e1418.

Blank HM, Perez R, He C, Maitra N, Metz R, Hill J, Lin Y, Johnson CD, Bankaitis VA, Kennedy BK, et al. (2017). Translational control of lipogenic enzymes in the cell cycle of synchronous, growing yeast cells. EMBO J 36, 487–502.

Carpy A, Krug K, Graf S, Koch A, Popic S, Hauf S, Macek B (2014). Absolute proteome and phosphoproteome dynamics during the cell cycle of Schizosaccharomyces pombe (Fission Yeast). Mol Cell Proteomics 13, 1925–1936.

Cho RJ, Campbell MJ, Winzeler EA, Steinmetz L, Conway A, Wodicka L, Wolfsberg TG, Gabrielian AE, Landsman D, Lockhart DJ, Davis RW (1998). A genome-wide transcriptional analysis of the mitotic cell cycle. Mol Cell 2, 65–73.

Christensen DG, Meyer JG, Baumgartner JT, D'Souza AK, Nelson WC, Payne SH, Kuhn ML, Schilling B, Wolfe AJ (2018). Identification of novel protein lysine acetyltransferases in Escherichia coli. mBio 9.

Collins BC, Hunter CL, Liu Y, Schilling B, Rosenberger G, Bader SL, Chan DW, Gibson BW, Gingras AC, Held JM, et al. (2017). Multi-laboratory assessment of reproducibility, qualitative and quantitative performance of SWATH-mass spectrometry. Nat Commun 8, 291.

Creanor J, Mitchison J (1979). Reduction of perturbations in leucine incorporation in synchronous cultures of Schizosaccharomyces pombe made by elutriation. J Gen Microbiol 112, 385–388.

Csardi G, Franks A, Choi DS, Airoldi EM, Drummond DA (2015). Accounting for experimental noise reveals that mRNA levels, amplified by post-transcriptional processes, largely determine steady-state protein levels in yeast. PLoS Genet 11, e1005206.

Dahl C, Biemann HP, Dahl J (1987). A protein kinase antigenically related to pp60v-src possibly involved in yeast cell cycle control: positive in vivo regulation by sterol. Proc Natl Acad Sci USA 84, 4012–4016.

Dai L, Zhao T, Bisteau X, Sun W, Prabhu N, Lim YT, Sobota RM, Kaldis P, Nordlund P (2018). Modulation of protein-interaction states through the cell cycle. Cell 173, 1481–1494.e1413.

de Lichtenberg U, Wernersson R, Jensen TS, Nielsen HB, Fausboll A, Schmidt P, Hansen FB, Knudsen S, Brunak S (2005). New weakly expressed cell cycle-regulated genes in yeast. Yeast 22, 1191–1201.

Dephoure N, Zhou C, Villen J, Beausoleil SA, Bakalarski CE, Elledge SJ, Gygi SP (2008). A quantitative atlas of mitotic phosphorylation. Proc Natl Acad Sci USA 105, 10762–10767.

Elliott SG, Warner JR, McLaughlin CS (1979). Synthesis of ribosomal proteins during the cell cycle of the yeast Saccharomyces cerevisiae. J Bacteriol 137, 1048–1050.

Evans T, Rosenthal ET, Youngblom J, Distel D, Hunt T (1983). Cyclin: a protein specified by maternal mRNA in sea urchin eggs that is destroyed at each cleavage division. Cell 33, 389–396.

Ewald JC, Kuehne A, Zamboni N, Skotheim JM (2016). The yeast cyclin-dependent kinase routes carbon fluxes to fuel cell cycle progression. Mol Cell 62, 532–545.

Flory MR, Lee H, Bonneau R, Mallick P, Serikawa K, Morris DR, Aebersold R (2006). Quantitative proteomic analysis of the budding yeast cell cycle using acid-cleavable isotope-coded affinity tag reagents. Proteomics 6, 6146–6157.

Frenkel-Morgenstern M, Danon T, Christian T, Igarashi T, Cohen L, Hou YM, Jensen LJ (2012). Genes adopt non-optimal codon usage to generate cell cycle-dependent oscillations in protein levels. Mol Syst Biol 8, 572.

Furse S, Shearman GC (2018). Do lipids shape the eukaryotic cell cycle? Biochim Biophys Acta Mol Cell Biol Lipids 1863, 9–19.

Gaber RF, Copple DM, Kennedy BK, Vidal M, Bard M (1989). The yeast gene ERG6 is required for normal membrane function but is not essential for biosynthesis of the cell-cycle-sparking sterol. Mol Cell Biol 9, 3447–3456.

Gasch AP, Spellman PT, Kao CM, Carmel-Harel O, Eisen MB, Storz G, Botstein D, Brown PO (2000). Genomic expression programs in the response of yeast cells to environmental changes. Mol Biol Cell 11, 4241–4257.

Giaever G, Chu AM, Ni L, Connelly C, Riles L, Veronneau S, Dow S, Lucau-Danila A, Anderson K, Andre B, et al. (2002). Functional profiling of the Saccharomyces cerevisiae genome. Nature 418, 387–391.

Gillet LC, Navarro P, Tate S, Rost H, Selevsek N, Reiter L, Bonner R, Aebersold R (2012). Targeted data extraction of the MS/MS spectra generated by data-independent acquisition: a new concept for consistent and accurate proteome analysis. Mol Cell Proteomics 11, O111.016717.

Granovskaia MV, Jensen LJ, Ritchie ME, Toedling J, Ning Y, Bork P, Huber W, Steinmetz LM (2010). High-resolution transcription atlas of the mitotic cell cycle in budding yeast. Genome Biol 11, R24.

Guo J, Bryan BA, Polymenis M (2004). Nutrient-specific effects in the coordination of cell growth with cell division in continuous cultures of Saccharomyces cerevisiae. Arch Microbiol 182, 326–330.

Hardy CD, Cozzarelli NR (2005). A genetic selection for supercoiling mutants of Escherichia coli reveals proteins implicated in chromosome structure. Mol Microbiol 57, 1636–1652.

Hasslacher M, Ivessa AS, Paltauf F, Kohlwein SD (1993). Acetyl-CoA carboxylase from yeast is an essential enzyme and is regulated by factors that control phospholipid metabolism. J Biol Chem 268, 10946–10952.

Ho B, Baryshnikova A, Brown GW (2018). Unification of protein abundance datasets yields a quantitative Saccharomyces cerevisiae proteome. Cell Systems 6, 192–205.e193.

Hoose SA, Rawlings JA, Kelly MM, Leitch MC, Ababneh QO, Robles JP, Taylor D, Hoover EM, Hailu B, McEnery KA, et al. (2012). A systematic analysis of cell cycle regulators in yeast reveals that most factors act independently of cell size to control initiation of division. PLoS Genet 8, e1002590.

Hopper AK (2013). Transfer RNA post-transcriptional processing, turnover, and subcellular dynamics in the yeast Saccharomyces cerevisiae. Genetics 194, 43–67.

Huang J, Mousley CJ, Dacquay L, Maitra N, Drin G, He C, Ridgway ND, Tripathi A, Kennedy M, Kennedy BK, et al. (2018). A Lipid transfer protein signaling axis exerts dual control of cell-cycle and membrane trafficking systems. Dev Cell 44, 378–391.e375.

Jorgensen P, Nishikawa JL, Breitkreutz BJ, Tyers M (2002). Systematic identification of pathways that couple cell growth and division in yeast. Science 297, 395–400.

Juppner J, Mubeen U, Leisse A, Caldana C, Brust H, Steup M, Herrmann M, Steinhauser D, Giavalisco P (2017). Dynamics of lipids and metabolites during the cell cycle of Chlamydomonas reinhardtii. Plant J 92, 331–343.

Kaiser C, Michaelis S, Mitchell A. (1994). Methods in Yeast Genetics: A Cold Spring Harbor Laboratory Course Manual. Cold Spring Harbor, NY: Cold Spring Harbor Laboratory Press.

Kettle E, Page SL, Morgan GP, Malladi CS, Wong CL, Boadle RA, Marsh BJ, Robinson PJ, Chircop M (2015). A cholesterol-dependent endocytic mechanism generates midbody tubules during cytokinesis. Traffic (Copenhagen, Denmark) 16, 1174–1192.

Kim Y, Kim EY, Seo YM, Yoon TK, Lee WS, Lee KA (2012). Function of the pentose phosphate pathway and its key enzyme, transketolase, in the regulation of the meiotic cell cycle in oocytes. Clin Exp Reprod Med 39, 58–67.

Kurat CF, Wolinski H, Petschnigg J, Kaluarachchi S, Andrews B, Natter K, Kohlwein SD (2009). Cdk1/Cdc28-dependent activation of the major triacylglycerol lipase Tgl4 in yeast links lipolysis to cell-cycle progression. Mol Cell 33, 53–63.

Lahtvee P.-J., Sánchez BJ, Smialowska A, Kasvandik S, Elsemman IE, Gatto F, Nielsen J (2017). Absolute quantification of protein and mRNA abundances demonstrate variability in gene-specific translation efficiency in yeast. Cell Systems 4, 495–504. e495.

Lane KR, Yu Y, Lackey PE, Chen X, Marzluff WF, Cook JG (2013). Cell cycle-regulated protein abundance changes in synchronously proliferating HeLa cells include regulation of pre-mRNA splicing proteins. PLoS One 8, e58456.

Larsson O, Sonenberg N, Nadon R (2011). anota: Analysis of differential translation in genome-wide studies. Bioinformatics 27, 1440–1441.

Liao Y, Smyth GK, Shi W (2019). The R package Rsubread is easier, faster, cheaper and better for alignment and quantification of RNA sequencing reads. Nucleic Acids Res 47, e47.

Lin Y, Liu H, Liu Z, Liu Y, He Q, Chen P, Wang X, Liang S (2013). Development and evaluation of an entirely solution-based combinative sample preparation method for membrane proteomics. Anal Biochem 432, 41–48.

Lindahl PE (1948). Principle of a counter-streaming centrifuge for the separation of particles of different sizes. Nature 161, 648.

Lodish HF (1974). Model for the regulation of mRNA translation applied to haemoglobin synthesis. Nature 251, 385–388.

Love MI, Huber W, Anders S (2014). Moderated estimation of fold change and dispersion for RNA-seq data with DESeq2. Genome Biol 15, 550.

Lu P, Vogel C, Wang R, Yao X, Marcotte EM (2007). Absolute protein expression profiling estimates the relative contributions of transcriptional and translational regulation. Nat Biotechnol 25, 117–124.

Ly T, Ahmad Y, Shlien A, Soroka D, Mills A, Emanuele MJ, Stratton MR, Lamond AI (2014). A proteomic chronology of gene expression through the cell cycle in human myeloid leukemia cells. Elife 3, e01630.

Ly T, Endo A, Lamond AI (2015). Proteomic analysis of the response to cell cycle arrests in human myeloid leukemia cells. eLife 4, e04534.

Maitra N, Anandhakumar J, Blank HM, Kaplan CD, Polymenis M (2019). Perturbations of transcription and gene expression-associated processes alter distribution of cell size values in Saccharomyces cerevisiae. G3 9, 239–250.

Mann M (2006). Functional and quantitative proteomics using SILAC. Nat Rev Mol Cell Biol 7, 952–958.

McCusker D, Kellogg DR (2012). Plasma membrane growth during the cell cycle: unsolved mysteries and recent progress. Curr Opin Cell Biol 24, 845–851.

Mitchison JM (1971). Synchronous cultures. In: The Biology of the Cell Cycle, New York: Cambridge University Press, 25–57.

Oliva A, Rosebrock A, Ferrezuelo F, Pyne S, Chen H, Skiena S, Futcher B, Leatherwood J (2005). The cell cycle-regulated genes of Schizosaccharomyces pombe. PLoS Biol 3, e225.

Olsen JV, Vermeulen M, Santamaria A, Kumar C, Miller ML, Jensen LJ, Gnad F, Cox J, Jensen TS, Nigg EA, et al. (2010). Quantitative phosphoproteomics reveals widespread full phosphorylation site occupancy during mitosis. Sci Signal 3, ra3.

Olshen AB, Hsieh AC, Stumpf CR, Olshen RA, Ruggero D, Taylor BS (2013). Assessing gene-level translational control from ribosome profiling. Bioinformatics 29, 2995–3002.

Peng J, Schwartz D, Elias JE, Thoreen CC, Cheng D, Marsischky G, Roelofs J, Finley D, Gygi SP (2003). A proteomics approach to understanding protein ubiquitination. Nature Biotechnol 21, 921–926.

Pramila T, Wu W, Miles S, Noble WS, Breeden LL (2006). The Forkhead transcription factor Hcm1 regulates chromosome segregation genes and fills the S-phase gap in the transcriptional circuitry of the cell cycle. Genes Dev 20, 2266–2278.

Pringle JR, Hartwell LH (1981). The Saccharomyces cerevisiae cell cycle. In: The Molecular and Cellular Biology of the Yeast Saccharomyces, Vol. 1, Cold Spring Harbor, NY: Cold Spring Harbor Laboratory Press, 97–142.

Rustici G, Mata J, Kivinen K, Lio P, Penkett CJ, Burns G, Hayles J, Brazma A, Nurse P, Bahler J (2004). Periodic gene expression program of the fission yeast cell cycle. Nat Genet 36, 809–817.

Sanchez-Alvarez M, Zhang Q, Finger F, Wakelam MJ, Bakal C (2015). Cell cycle progression is an essential regulatory component of phospholipid metabolism and membrane homeostasis. Open Biol 5, 150093.

Santos A, Wernersson R, Jensen LJ (2015). Cyclebase 3.0: a multi-organism database on cell-cycle regulation and phenotypes. Nucleic Acids Res 43, D1140–D1144.

Scaglia N, Tyekucheva S, Zadra G, Photopoulos C, Loda M (2014). De novo fatty acid synthesis at the mitotic exit is required to complete cellular division. Cell Cycle 13, 859–868.

Schilling B, Gibson BW, Hunter CL (2017). Generation of high-quality SWATH((R)) acquisition data for label-free quantitative proteomics studies using TripleTOF((R)) mass spectrometers. Methods Mol Biol 1550, 223–233.

Schillinger J, Severin K, Kaschani F, Kaiser M, Ehrmann M (2018). HTRA1-dependent cell cycle proteomics. J Proteome Res 17, 2679–2694.

Schneiter R, Hitomi M, Ivessa AS, Fasch EV, Kohlwein SD, Tartakoff AM (1996). A yeast acetyl coenzyme A carboxylase mutant links very-long-chain fatty acid synthesis to the structure and function of the nuclear membrane-pore complex. Mol Cell Biol 16, 7161–7172.

Shulman RW, Hartwell LH, Warner JR (1973). Synthesis of ribosomal proteins during the yeast cell cycle. J Mol Biol 73, 513–525.

Singh P, Saxena R, Srinivas G, Pande G, Chattopadhyay A (2013). Cholesterol biosynthesis and homeostasis in regulation of the cell cycle. PLoS One 8, e58833.

Soma S, Yang K, Morales MI, Polymenis M (2014). Multiple metabolic requirements for size homeostasis and initiation of division in Saccharomyces cerevisiae. Microb Cell 1, 256–266.

Spellman PT, Sherlock G, Zhang MQ, Iyer VR, Anders K, Eisen MB, Brown PO, Botstein D, Futcher B (1998). Comprehensive identification of

cell cycle-regulated genes of the yeast Saccharomyces cerevisiae by microarray hybridization. Mol Biol Cell 9, 3273–3297.

Suarez Y, Fernandez C, Ledo B, Ferruelo AJ, Martin M, Vega MA, Gomez-Coronado D, Lasuncion MA (2002). Differential effects of ergosterol and cholesterol on Cdk1 activation and SRE-driven transcription. Eur J Biochem 269, 1761–1771.

Swaffer MP, Jones AW, Flynn HR, Snijders AP, Nurse P (2016). CDK substrate phosphorylation and ordering the cell cycle. Cell 167, 1750–1761.e1716.

Swaney DL, Beltrao P, Starita L, Guo A, Rush J, Fields S, Krogan NJ, Villen J (2013). Global analysis of phosphorylation and ubiquitylation cross-talk in protein degradation. Nat Methods 10, 676–682.

Torrent M, Chalancon G, de Groot NS, Wuster A, Madan Babu M (2018). Cells alter their tRNA abundance to selectively regulate protein synthesis during stress conditions. Sci Signal 11.

Truong SK, McCormick RF, Polymenis M (2013). Genetic determinants of cell size at birth and their impact on cell cycle progression in Saccharomyces cerevisiae. G3 3, 1525–1530.

Tumu S, Patil A, Towns W, Dyavaiah M, Begley TJ (2012). The gene-specific codon counting database: a genome-based catalog of one-, two-, three-, four- and five-codon combinations present in Saccharomyces cerevisiae genes. Database (Oxford) 2012, bas002.

Vogel C, Marcotte EM (2012). Insights into the regulation of protein abundance from proteomic and transcriptomic analyses. Nat Rev Genet 13, 227–232.

Warner JR (1999). The economics of ribosome biosynthesis in yeast. Trends Biochem Sci 24, 437–440.

Weinberg DE, Shah P, Eichhorn SW, Hussmann JA, Plotkin JB, Bartel DP (2016). Improved ribosome-footprint and mrna measurements provide insights into dynamics and regulation of yeast translation. Cell Rep 14, 1787–1799.

Wilcox RR (2011). Introduction to robust estimation and hypothesis testing, New York: Academic Press.

Wisniewski JR, Zougman A, Nagaraj N, Mann M (2009). Universal sample preparation method for proteome analysis. Nat Methods 6, 359–362.

Yang PL, Hsu TH, Wang CW, Chen RH (2016). Lipid droplets maintain lipid homeostasis during anaphase for efficient cell separation in budding yeast. Mol Biol Cell 27, 2368–2380.

Zhang J, Schneider C, Ottmers L, Rodriguez R, Day A, Markwardt J, Schneider BL (2002). Genomic scale mutant hunt identifies cell size homeostasis genes in S. cerevisiae. Curr Biol 12, 1992–2001.

Zhao G, Chen Y, Carey L, Futcher B (2016). Cyclin-dependent kinase co-ordinates carbohydrate metabolism and cell cycle in S. cerevisiae. Mol Cell 62, 546–557.